Free Wake Panel Method Simulations of a Highly Flexible Wing at Flutter

Pinto Ribeiro, A.; Casalino, D.; Ferreira, Carlos

DOI
10.2514/6.2022-3595

Publication date
2022

Document Version
Final published version

Published in
AIAA AVIATION 2022 Forum

AIAA AVIATION Forum
June 27-July 1, 2022, Chicago, IL & Virtual
AIAA AVIATION 2022 Forum

10.2514/6.2022-3595

Free Wake Panel Method Simulations of a Highly Flexible Wing at Flutter

André F. P. Ribeiro*, Damiano Casalino†, and Carlos Ferreira‡
Delft University of Technology, Delft, The Netherlands

This paper shows fluid structure interaction simulations of a highly flexible wing at various flow conditions, including flutter regime. This is achieved with two-way time domain coupling of a geometrically exact beam structural model and a 3D free wake panel method, modelling the outer surface of the wing, which allow for non-linear effects of the geometry deformation and the flow to be taken into account. Static and aeroelastic wing deflections are compared to experimental data of the Pazy wing with good accuracy. Two regions of flutter onset are predicted within the experimental range. An analysis of the flutter modes is performed. This serves as a step towards mid-fidelity simulations for more complex configurations, including fuselage effects and tail interactions.

I. Nomenclature

CFD	=	computational fluid dynamics	G	=	shear modulus
DLM	=	doublet lattice method	γ	=	wake vortex strength
FEM	=	finite element method	I	=	inertia
VLM	=	vortex lattice method	K	=	stiffness
A	=	area	m	=	mass
A_{ij}	=	doublets influence coefficient matrix	μ	=	doublet strength
α	=	angle of attack	$\hat{n}$	=	surface normal
B_{ij}	=	sources influence coefficient matrix	S	=	wing span
C_{ij}	=	wake vortices influence coefficient matrix	σ	=	source strength
c	=	wing chord	$\vec{T}$	=	torque
c_1, c_2, c_3	=	lumped mass distance to node	θ	=	rotation around y axis
$\vec{d}$	=	direction of beam element	$\vec{U}_b$	=	body velocity
Δt	=	timestep	U_∞	=	freestream velocity
E	=	Young's modulus	u	=	displacement in x axis
$\vec{F}$	=	force	w	=	displacement in z axis
Φ	=	velocity potential	$\vec{x}$	=	position vector
Φ_∞	=	freestream velocity potential			

II. Introduction

With the increase in popularity of low speed, very high aspect ratio, highly flexible wings, the importance of nonlinear aeroelastic methods has increased. Models that can accurately include the large deflections into stability calculations of these aircraft are needed to avoid late stage failures in the development cycle. In order to validate such models, the Pazy wing experiment [1] was conducted as part of the Aeroelastic Prediction Workshop (AePW) Large Deflection Working Group [2–4]. This is a simple, yet challenging test case, as the non-linearities have substantial effects on the structural and aeroelastic properties of the wing, with "some trends that are opposite to those obtained in the linear domain" [5].

Several groups have simulated the Pazy wing, typically with linearized methods [6], as adding structural and aerodynamic non-linearities is considered demanding [7]. The linearization needs to be done on the deformed

*PhD Candidate, Wind Energy, A.PintoRibeiro@tudelft.nl, AIAA Member.
†Chairholder Aeroacoustics, Wind Energy, D.Casalino@tudelft.nl
‡Chairholder Wind Energy Science, Wind Energy, C.J.SimaoFerreira@tudelft.nl

configuration, i.e., after statically deforming the wing for certain flow conditions, to deal with the aforementioned non-linearities [8]. Computational fluid dynamics (CFD) has the potential to perform such calculations in a fully non-linear framework, but the computational cost is still too high for the quick turnaround required during the design phase.

Panel methods have shown good balance between accuracy and cost for the simulation of flexible wings [9]. Typically, the vortex lattice method (VLM) or doublet lattice methods (DLM) are employed for aeroelastic simulations of wings [8]. These methods employ a panel sheet running through the wing chord line, hence thickness effects are neglected. A major drawback of using panel sheets is the difficulty describing aircraft fuselages and other bodies that can have an effect on the wing aerodynamics, such as wing mounted pods.

An alternative to VLM and DLM is a full 3D panel method, where the complete surface of the aircraft is modelled. This allows for thickness effects to be captured, for boundary layer models to be included, and for a one-to-one correspondence with CFD results, so that corrections can be easily implemented in the panel code based on CFD simulations, that can capture transition effects, separations, and shocks. Loads on fuselages can also be calculated more accurately, as their surfaces are represented in their entirety.

In this work, we seek to contribute to the Pazy wing and the AePW by conducting fully non-linear, time domain simulations. A 3D free wake panel method is used, coupled with a geometrically exact beam structural model.

III. Numerical Methods

A. Aerodynamics

We employ a source and doublet panel method with free-wakes [10] in order to capture the aerodynamics of the flexible wing. The thickness effects are fully captured, as the triangular or quadrilateral panels lie on the wing surface. The surface and wake discretization of the velocity potential equation leads to the following linear system:

$$\frac{1}{4\pi}A_{ij}\mu_j + \frac{1}{4\pi}B_{ij}\sigma_j + \frac{1}{4\pi}C_{iw}\gamma_w = 0 \tag{1}$$

where A_{ij}, B_{ij}, and C_{ij} are the influence coefficients matrices [11] for the doublets μ, sources σ, and wake vortices γ respectively. The values of μ, σ, and γ are constant over each panel. A far-field formulation can be used to make the calculations of the influence coefficients substantially faster when computing A_{ij}, B_{ij}, and C_{ij} over large distances [11]. The sources σ are computed to ensure impermeability, with:

$$\sigma = -(\vec{U}_\infty - \vec{U}_b)\cdot\hat{n} \tag{2}$$

where $\vec{U}_\infty$ is the freestream velocity, $\vec{U}_b$ is the local kinematic velocity of the body, due to aeroelastic effects, and $\hat{n}$ is the surface normal. The wake vortices can be computed based on the doublets intensities on the top (t) and bottom (b) of the trailing edge, following the Kutta condition:

$$\gamma = \mu^t - \mu^b - (\Phi^t_\infty - \Phi^b_\infty) \tag{3}$$

where $\Phi_\infty = \vec{U}_\infty \cdot \vec{x}$ is the freestream potential at an arbitrary location $\vec{x}$, which in this case are the center of the top and bottom panels. The term in parentheses is often neglected, but is critical when simulating thick geometries using coarse meshes [12]. At every timestep, wake vortices are convected due to the freestream velocity and the induction of all the surface and wake panels. Wake-body interaction capabilities [13] and a vortex core model [14] are implemented, but not used for this study, as the wake panels do not intersect the wing after they are released. Combining Equations 1, 2, and 3, we are left with a square linear system with the doublets μ as unknowns. We solve this system either by direct matrix inversion or by the generalized minimal residual method.

We employ virtual panels in order to simulate symmetry planes [10], which dramatically reduce the influence coefficients matrices. With the linear system solved, surface velocities $\vec{U}$ are computed based on the basic potential flow equation, $\vec{U} = -\nabla\Phi$, where Φ is the velocity potential. The surface gradient is computed with central differences for quadrangular panels, but a least squares approximation [15, 16] is also available, and is always used for triangular panels. With the surface velocity available, the unsteady Bernoulli equation [17] is used to find the surface pressure, which is then integrated over all surface panels to find the forces and moments acting on the bodies. The time derivatives in the unsteady Bernoulli equation and the value of $\vec{U}_b$ are calculated with a first order backwards Euler method.

B. Structural Model

The structural deformation of the wing is computed with a geometrically exact beam model [18, 19]. This allows for non-linear, time domain calculations with large deflections, anisotropic deformation couplings, and curved beams. The open source GXBeam Julia module [20] is used. The structural properties of the beam model were computed with the University of Michigan's Nonlinear Aeroelastic Simulation Toolbox (UM/NAST [3]), by matching the structural properties of a detailed 3D finite element method (FEM) wing model. The beam has 16 equally spaced nodes. The elements are Timoshenko beams, requiring 6×6 symmetric stiffness matrices:

$$\begin{bmatrix} EA & 0 & 0 & K_{12} & K_{13} & K_{14} \\ 0 & GA & 0 & 0 & 0 & 0 \\ 0 & 0 & GA & 0 & 0 & 0 \\ K_{12} & 0 & 0 & K_{22} & K_{23} & K_{24} \\ K_{13} & 0 & 0 & K_{23} & K_{33} & K_{34} \\ K_{14} & 0 & 0 & K_{24} & K_{34} & K_{44} \end{bmatrix} \tag{4}$$

where E is Young's modulus, A is the cross-section area, G is the shear modulus (assumed to be very large), K is the stiffness, and the indices 1, 2, 3, and 4 correspond to the axial, torsion, out of plane bending (flapping), and in plane bending (edge-wise) displacements. The inertial effects are accounted for with 6×6 symmetric inertia matrices. UM/NAST provides node-based inertia matrices, defined as:

$$\begin{bmatrix} m & 0 & 0 & 0 & mc_3 & -mc_4 \\ 0 & m & 0 & -mc_3 & 0 & mc_1 \\ 0 & 0 & m & mc_4 & -mc_1 & 0 \\ 0 & -mc_3 & mc_4 & I_{22} & -I_{32} & I_{24} \\ mc_3 & 0 & -mc_1 & -I_{32} & I_{33} & -I_{34} \\ -mc_4 & mc_1 & 0 & I_{24} & -I_{34} & I_{44} \end{bmatrix} \tag{5}$$

where m is the lumped mass, c is the distance of the lumped mass to the beam node, and I the inertia, with indices consistent with the stiffness matrix. GXBeam has limitations for time domain simulations using node-based inertia matrices. This makes aeroelastic simulations unstable, and hence an element-based method can be used. This is achieved by dividing the node-based inertia matrices by the element length, and assigning the inertia to the elements. We perform this by simply assigning half the inertia of each node to each adjacent element, with the first and last elements being assigned the full inertia of the first and last nodes.

C. Fluid Structure Interaction

The coupling of the aerodynamics and structural solvers is performed to allow for fluid structure interaction (FSI) simulations. Each surface panel i is associated with a structural node j, which is part of a beam model. This is done by nearest neighbor interpolation. Then, the force acting on each panel $\vec{F}_i$ is added to the corresponding nodes. The torque associated with each force $\vec{T}_i = (\vec{x}_i - \vec{x}_j) \times \vec{F}_i$, where $\vec{x}_i$ is the panel center and $\vec{x}_j$ is the node coordinates vector, is also added to each node. These forces and torques are inputs to the structural solver, which in turn computes the displacement and rotation of each node of the beam model.

The geometry involved in the FSI coupling is shown in Fig. 1. Each structural node n_j has an associated direction $\vec{d}_j$, which is constructed as the difference between the next and previous nodes coordinates. Each surface vertex i is projected onto the beam by $d_i = (\vec{x}_i - \vec{x}_j) \cdot \vec{d}_j$, where d_i is the projected distance to the structural nodes. Splines [21] are constructed to interpolate the displacements and rotations along the beam element, so that smooth distributions are available along the span. Then, each surface point is rotated and translated around the beam model, based on those splines. This morphs the geometry into its new shape, while preserving a smooth panel distribution.

The influence coefficients are recomputed at every timestep, to account for relative motion between the panels. The only non-linear effects that the current implementation neglects are related to flow separations, as the aerodynamic model is inviscid and hence unable to capture static or dynamic stall.

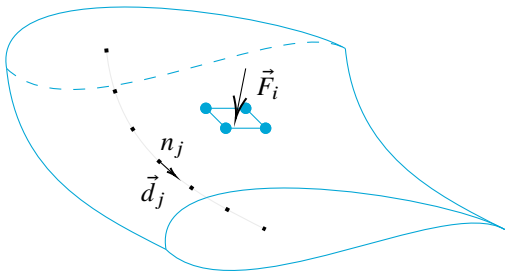

Fig. 1 Example of an aerodynamic section and panel (in blue) and the beam model nodes (black).

IV. Test Case Description

The Pazy wing [1] is a highly flexible wing constructed specifically for validation of aeroelastic models. It is a simple cantilevered rectangular wing composed of a NACA0018 airfoil with chord $c = 0.1$ m and span $S = 0.558$ m. Tip deflections of approximately half of the span were reached in the experiments. Flutter involving the second out of plane bending mode and first torsion mode is observed at relatively low speeds, while higher speeds develop flutter with the first out of plane bending mode and first torsion mode. The second flutter mode is particularly challenging to capture with linearized methods, as the wing is highly deformed [8]. At such deformation levels, influence coefficients need to be recomputed.

The wing skin is made of a flexible material and is deformed between the ribs and buckles at large wing deformations, adding some uncertainty to the aerodynamics of the wing and structural properties of the skin. While many simulations of the Pazy wing computed results using the structural model of the wing with and without the skin, as a way to estimate the experimental uncertainty [8], we focus on the experimental data with skin only, for clarity. It is worth noting that given a very detailed surface geometry of the wing with the deformed skin, the 3D panel method used in this work could include its aerodynamic effects, keeping in mind the limitations of the inviscid approach.

We model the Pazy wing using quadrilateral panels, with 150 panels in the chordwise direction with a cosine distribution, and 26 panels in the spanwise direction, with a uniform distribution. The surface mesh is shown in Fig. 2, along with the coordinate system definition used in this work. A symmetry plane is placed on the wing root to model the wind tunnel wall. The timestep is set to $\Delta t = 0.5c/U_\infty$. Wake panels are deleted once they reach the arbitrary location of $x = 10S$, as this saves computational time and did not affect the results. Simulations are run for at least 1000 timesteps, or 500 flow passes, where the first 4 timesteps are used to initialize the wake, with a rigid wing. Cases where flutter occurred were run until the structural solver diverged, which usually happened after thousands of timesteps. Detecting the presence of flutter could be done early in the simulation, as will be shown in Section V.B.

Fig. 2 Surface mesh of the Pazy wing, seen from the root side.

V. Results

A. Structural Model Validation

We start by validating the structural model without the aerodynamics. The experimental data set includes static wing deformation, achieved by placing a weight at the wing tip. Two cases are investigated: with the weight applied near the elastic center, and with a lever arm of 0.13 m, dubbed the bend and the torsion tests, respectively. The wing tip vertical displacement w is shown in Fig. 3, corresponding to the bend test. The wing tip twist θ from the torsion test is shown in Fig. 4. Numerical data computed with the full FEM model used to calibrate the beam model used in this work are shown for the bend test. Results match well with the full FEM model, with some discrepancies with experimental data for high values of tip mass. The twist behaves in a similar fashion, with some uncertainty associated with twist angles for large values of w, as defining the twist becomes somewhat subjective. Here, we measure θ by projecting the tip leading and trailing edges on a vertical plane.

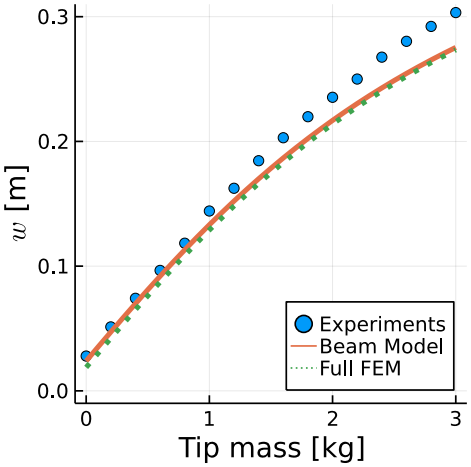

Fig. 3 Static wing bend test results. Vertical tip displacement versus mass placed at wing tip.

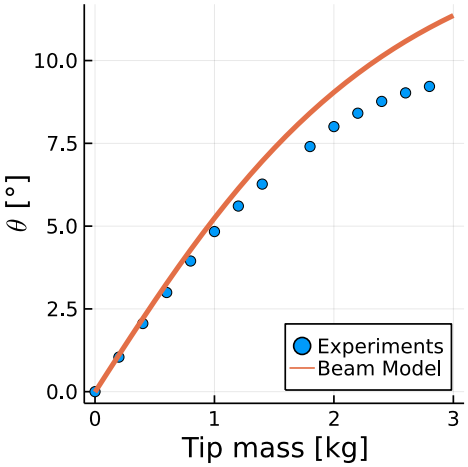

Fig. 4 Static wing torsion test results. Tip twist angle versus mass placed at wing tip, behind the trailing edge.

The natural frequencies of the model are shown in Table 1, where "bending" stands for the out of plane bending mode and "horizontal" stands for the in plane bending mode. The frequencies are compared with results provided by the University of Michigan [3], who calculated stiffness and inertia matrices for the beam model used in this work. The two codes agree very well when the node-based inertia is used in GXBeam, as this is the same approach taken by the University of Michigan. When using element-based inertia, discrepancies up to 5% in the natural frequencies can be observed. Due to the aforementioned limitations of GXBeam, we use the element-based approach for the remainder of this work, in spite of these discrepancies.

Table 1 Natural frequencies (Hz) of the wing beam model

Mode	Description	Element-based	Node-based	UM/NAST [3]
1	1st bending	4.23	4.19	4.19
2	2nd bending	29.31	28.50	28.49
3	1st torsion	42.12	42.02	41.88
4	3rd bending	87.11	83.11	83.06
5	1st horizontal	106.13	105.22	105.89

B. Aeroelastic Simulations Validation

Aeroelastic simulations were conducted for angles of attack $\alpha = 3$, 5, and 7°, with U_∞ varying from 20 to 80 m/s. Figures 5 and 6 show the time history of the wing tip twist angle θ for four different simulations. At $U_\infty = 45$ and 75 m/s, oscillations appear early in the simulations ($tU_\infty/c = 100$), but they are damped and θ ultimately converges to a single value. For $U_\infty = 50$ m/s, θ diverges as the wing encounters the first flutter mode. The same happens at $U_\infty = 80$ m/s for the second flutter mode. Oscillations for the second flutter mode clearly occur at much lower frequencies and higher amplitudes than the first, as the second flutter mode is associated with the first bending mode and the first flutter mode is associated with the second bending mode. Note that from here on, θ is simply the angle around the y axis, as computed by the structural model, hence ignoring the small contribution from rotation around the z axis.

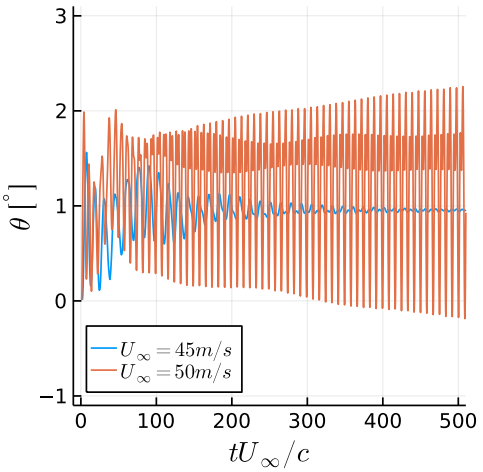

Fig. 5 Time history of wing tip twist for α = 3° near and at the first flutter mode.

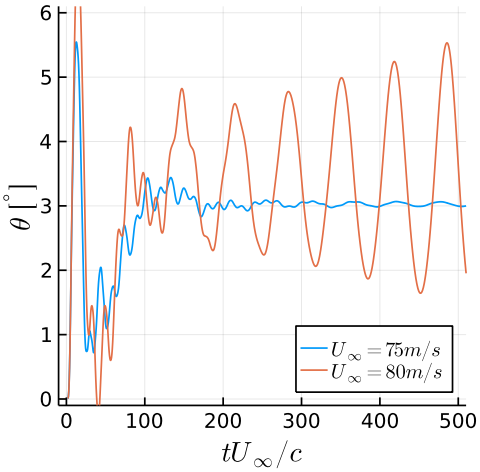

Fig. 6 Time history of wing tip twist for α = 3° near and at the second flutter mode.

The Pazy flutter boundaries were measured by recent experiments [4] where two regions could be extracted: a smaller onset region and a larger offset region. For example, at 3 deg, if the flow speed was continuously increased, the wing would start vibrating at 49 m/s. Once the vibrations started, a hysteresis effect would mean that decelerating to 40 m/s was required to stop them. Interestingly, the onset region matched numerical predictions [5] very well. These results correspond to the first flutter region, which involves the first torsion and second bending modes. Increasing the flow speed made the vibrations disappear. At much higher flow speeds, a second flutter region appears, involving the first torsion and first bending modes. The experimental flutter boundary for the second flutter region is not yet available, hence numerical data is used for reference.

Figure 7 shows the vertical tip displacement of the wing w as a function of the freestream velocity U_∞ for $\alpha = 3$, 5, and 7°. The blue diamonds represent the experimental first flutter onset region, i.e., the velocities in which the wing enters flutter. The area shaded in blue represents the experimental first flutter offset, that is, once the wing starts to flutter, it needs to go outside that range of U_∞ for flutter to stop. Note that for $\alpha = 7°$ there was no experimental data for reducing U_∞, hence the upper range of the flutter onset and lower range of the flutter offset are unknown. The dotted blue lines present for $\alpha = 5$ and 7° represent the experimental mean deformation of the wing. The green diamonds show the second flutter onset region found with SHARPy [8] for the Pre-Pazy wing, which is slightly different from the Pazy wing simulated here, but serves as the best current estimate of the second flutter onset. The orange circles represent simulations with the present panel method, while the stars highlight cases for which the simulations diverged, as shown in Figs. 5 and 6.

The results in Fig 7 show an excellent agreement between the present methods and the references. The mean tip deflection matches the experimental data very well. The first flutter onset region is within the experimental range and the second flutter onset region matches the SHARPy results. In this work, the objective was to find the conditions that create flutter, rather than trying to characterize the limit cycle oscillations (LCO). After some time with the wing under strong vibrations, the structural solver would diverge in these simulations, and we did not attempt to stabilize it, as this was enough for us to consider that the case had begun to flutter.

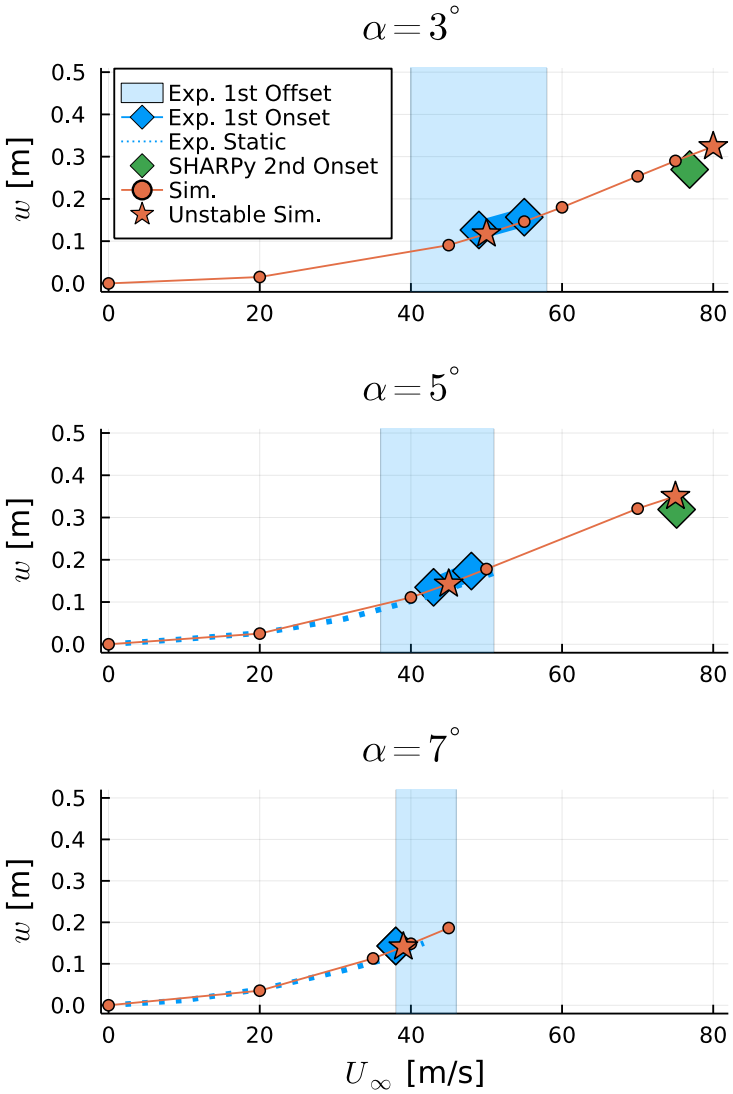

Fig. 7 Vertical tip displacement range for various flow velocities at three angles of attack.

C. Flutter Characteristics

We turn our attention to two specific cases of the previous section: $U_\infty = 50$ and 80 m/s at $\alpha = 3°$. These cases produced the first and second flutter modes of the Pazy wing, respectively. We seek to characterize the flutter motion in Figs. 8 and 9. The second flutter mode, shown in Fig. 8 is displaying a vertical displacement that is in opposite phase with the wing twist, while being ahead of it. The entire wing is bending and twisting in the same direction, confirming this is indeed a combination of the first bending and first twisting modes. The horizontal displacement is in phase with the wing twist and at the same frequency. This quasi-steady relation with the twist angle indicates the first horizontal bending mode is not playing a role here.

Figure 9 shows the same analysis on the first bending mode. Consistent with the experimental analysis [4], the vertical displacement (which is changing signs around 85% of the span) corresponds to the second bending mode and is in phase with the twist, and ahead of it (as evidenced by the trough for $w - \bar{w}$ at $tU_\infty/c = 516$ and the trough for θ at $tU_\infty/c = 517$). Again the horizontal motion seems to follow the twist. Unlike the experimental data, a second torsion mode seems to be present. As the structural model for this case was not tuned to have the correct second torsion mode, this is likely not something that would occur in reality. It might also be related to the element-based inertia matrices used in GXBeam. The second torsion mode is almost in phase with the first, but the lag between them changes

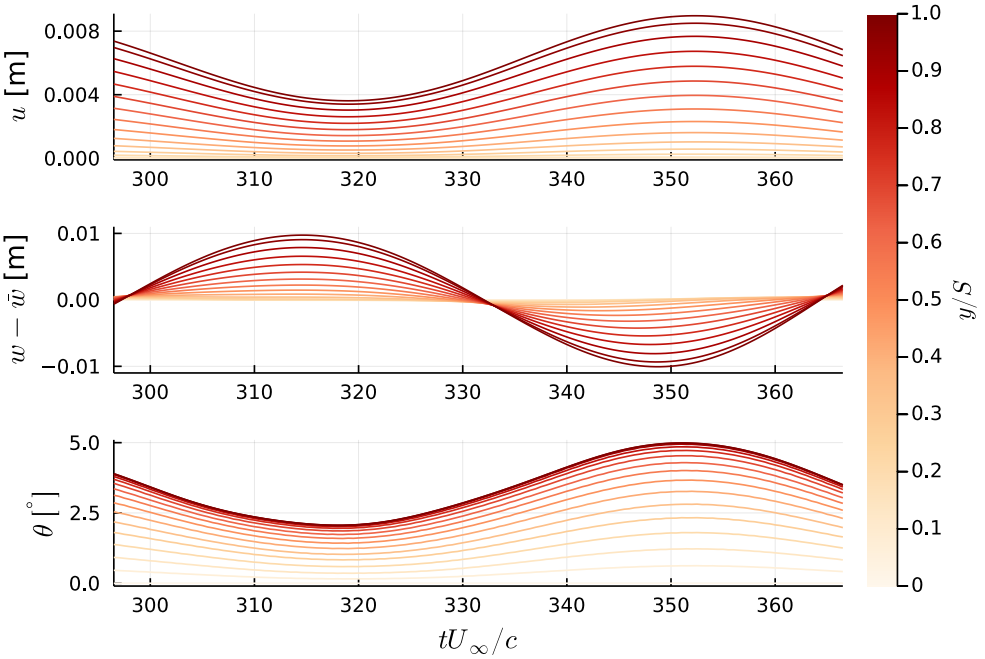

Fig. 8 Horizontal displacement along the wing (top), vertical displacement fluctuation along the wing (middle), and twist angle along the wing (bottom) for $\alpha = 3°$, $U_\infty = 80$ m/s, at the second flutter mode. Colors represent the spanwise position.

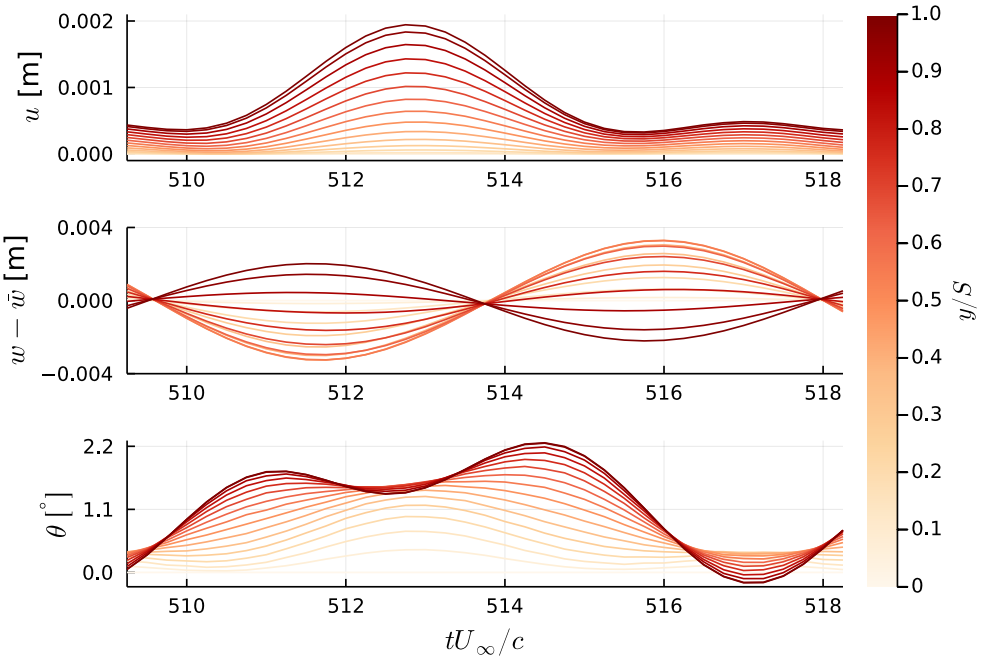

Fig. 9 Horizontal displacement along the wing (top), vertical displacement fluctuation along the wing (middle), and twist angle along the wing (bottom) for $\alpha = 3°$, $U_\infty = 50$ m/s, at the first flutter mode. Colors represent the spanwise position.

throughout the simulations, sometimes reducing the peak in the twist curves, sometimes amplifying it. Ignoring the second torsion mode, the results shown in Fig. 9 are very similar to experimental data shown in [4].

Finally, in Figs. 10 and 11 we can see the Pazy wing, along with its wake, for the first and second flutter modes, respectively. The wakes are colored by the vortex strength γ, which is proportional to the sectional circulation, and hence, lift coefficient, at the time the wake panel is shed. The second flutter mode, shown in Fig. 11, occurs at very large levels of wing deformation. White regions on the wake indicate high sectional lift and we can see two white spots, one near the wing and one at 60% of the wake length, showing the low frequency of the wing oscillations. The first flutter mode, on Fig. 10, is clearly occurring at a much higher frequency. As the second bending mode is active, the color patters on the wake are more complex, as the lift along the wing is not fluctuating in a synchronized fashion. We can also observe the wake structures becoming larger and more complex as they move downstream, as one would expect from a plunging airfoil [22].

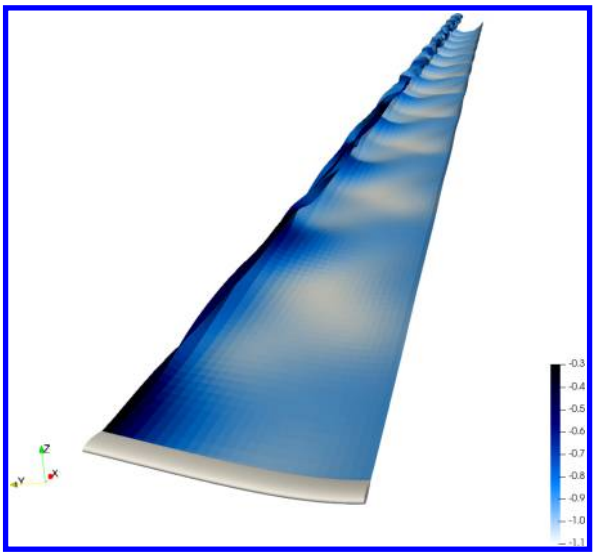

Fig. 10 Pazy wing and its wake, colored by vortex strength, at $\alpha = 3°$, $U_\infty = 50$ m/s. First flutter mode.

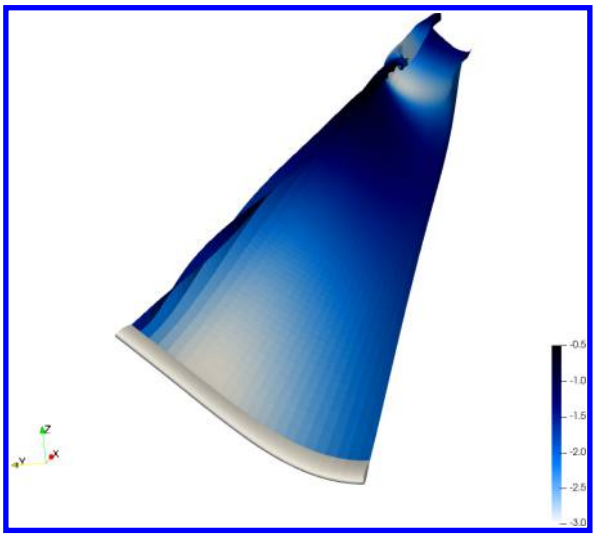

Fig. 11 Pazy wing and its wake, colored by vortex strength, at $\alpha = 3°$, $U_\infty = 80$ m/s. Second flutter mode.

VI. Conclusions

Simulations of the Pazy wing were conducted for different angles of attack and flow velocities. The structural model and the aeroelastic simulations were compared with experimental data, with good agreement being found between simulations and experiments. In particular, the flutter onset was predicted within the range of experimental values. An analysis of the flutter motion was done, in order to clarify the phenomena occurring at the first and second flutter modes.

The framework developed herein can be applied to other, more complex cases in the future, where the advantages of a full 3D panel method would be more evident. Such cases can include fuselage-mounted wings, wings with pods, or aircraft where the wing wake has strong interactions with the horizontal tail plane.

Future simulations of the Pazy wing with the current method can include more geometrical details, such as the wing tip rod, and the deformed wing skin. With a detailed structural model, the deformation of the wing skin could be done within the simulations. More analysis of the second flutter mode can also be done, as doing so experimentally would likely break the wing.

Acknowledgments

The authors are grateful to Markus Ritter and Arik Drachinsky of the AePW Large Deflections Working Group, for their valuable feedback and assistance. We also acknowledge the help of Philipp Drescher and Daniella Raveh, for providing the FEM results and information on the Pazy wing, respectively. The structural solver used in this work is GXBeam and we are thankful to Taylor McDonnell, its developer, for support in its use.

References

[1] Avin, O., Raveh, D. E., Drachinsky, A., Ben-Shmuel, Y., and Tur, M., *An Experimental Benchmark of a Very Flexible Wing*, 2021. https://doi.org/10.2514/6.2021-1709.

[2] Ritter, M., and Hilger, J., *Dynamic Aeroelastic Simulations of the Pazy Wing by UVLM with Nonlinear Viscous Corrections*, 2022. https://doi.org/10.2514/6.2022-0177.

[3] Riso, C., and Cesnik, C. E., *Low-Order Geometrically Nonlinear Aeroelastic Modeling and Analysis of the Pazy Wing Experiment*, 2022. https://doi.org/10.2514/6.2022-2313.

[4] Drachinsky, A., Avin, O., Raveh, D. E., Ben-Shmuel, Y., and Tur, M., *Flutter Tests of the Pazy Wing*, 2022. https://doi.org/10.2514/6.2022-2186.

[5] Drachinsky, A., and Raveh, D. E., "Nonlinear Aeroelastic Analysis of Highly Flexible Wings Using the Modal Rotation Method," *AIAA Journal*, 2021, pp. 1–13. https://doi.org/10.2514/1.J061065.

[6] Ritter, M., Hilger, J., and Zimmer, M., *Static and Dynamic Simulations of the Pazy Wing Aeroelastic Benchmark by Nonlinear Potential Aerodynamics and detailed FE Model*, 2021. https://doi.org/10.2514/6.2021-1713.

[7] Righi, M., *Uncertainties Quantification in Flutter Prediction of a Wind Tunnel Model Exhibiting Large Displacements*, 2021. https://doi.org/10.2514/6.2021-1037.

[8] Goizueta, N., Drachinsky, A., Wynn, A., Raveh, D. E., and Palacios, R., *Flutter predictions for very flexible wing wind tunnel test*, 2021. https://doi.org/10.2514/6.2021-1711.

[9] Yang, L., Xie, C., and Yang, C., "Geometrically exact vortex lattice and panel methods in static aeroelasticity of very flexible wing," *Proceedings of the Institution of Mechanical Engineers, Part G: Journal of Aerospace Engineering*, Vol. 234, No. 3, 2020, pp. 742–759. https://doi.org/10.1177/0954410019885238.

[10] Katz, J., and Plotkin, A., *Low-Speed Aerodynamics*, 2nd ed., Cambridge Aerospace Series, Cambridge University Press, 2001. https://doi.org/10.1017/CBO9780511810329.

[11] Maskew, B., "Program VSAERO Theory Document: A Computer Program for Calculating Nonlinear Aerodynamic Characteristics of Arbitrary Configurations," Contractor Report 4023, National Aeronautics and Space Administration, 1987. URL https://ntrs.nasa.gov/citations/19900004884.

[12] Youngren, H., Bouchard, E., Coopersmith, R., and Miranda, L., *Comparison of panel method formulations and its influence on the development of QUADPAN, an advanced low-order method*, 1983. URL https://doi.org/10.2514/6.1983-1827.

[13] Gennaretti, M., and Bernardini, G., "Novel Boundary Integral Formulation for Blade-Vortex Interaction Aerodynamics of Helicopter Rotors," *AIAA Journal*, Vol. 45, No. 6, 2007, pp. 1169–1176. https://doi.org/10.2514/1.18383.

[14] Ramasamy, M., and Leishman, J. G., "A Reynolds Number-Based Blade Tip Vortex Model," *Journal of the American Helicopter Society*, Vol. 52, No. 3, 2007, pp. 214–223. https://doi.org/doi:10.4050/JAHS.52.214.

[15] Anderson, W. K., and Bonhaus, D. L., "An implicit upwind algorithm for computing turbulent flows on unstructured grids," *Computers & Fluids*, Vol. 23, No. 1, 1994, pp. 1–21. https://doi.org/10.1016/0045-7930(94)90023-X.

[16] Sozer, E., Brehm, C., and Kiris, C. C., "Gradient Calculation Methods on Arbitrary Polyhedral Unstructured Meshes for Cell-Centered CFD Solvers," *52nd Aerospace Sciences Meeting*, AIAA, 2014. https://doi.org/10.2514/6.2014-1440.

[17] Bernardini, G., Serafini, J., Molica Colella, M., and Gennaretti, M., "Analysis of a structural-aerodynamic fully-coupled formulation for aeroelastic response of rotorcraft," *Aerospace Science and Technology*, Vol. 29, No. 1, 2013, pp. 175–184. URL https://doi.org/10.1016/j.ast.2013.03.002.

[18] Yu, W., and Blair, M., "GEBT: A general-purpose nonlinear analysis tool for composite beams," *Composite Structures*, Vol. 94, No. 9, 2012, pp. 2677–2689. https://doi.org/10.1016/j.compstruct.2012.04.007.

[19] Wang, Q., and Yu, W., "Geometrically nonlinear analysis of composite beams using Wiener-Milenković parameters," *Journal of Renewable and Sustainable Energy*, Vol. 9, No. 3, 2017, p. 033306. https://doi.org/10.1063/1.4985091.

[20] "GXBeam," https://github.com/byuflowlab/GXBeam.jl, 2022. Accessed: April 13 2022.

[21] Dierckx, P., *Curve and Surface Fitting with Splines*, Monographs on numerical analysis, Clarendon Press, 1995. URL https://books.google.com/books?id=-RIQ3SR0sZMC.

[22] Young, J., and Lai, J. C. S., "Oscillation Frequency and Amplitude Effects on the Wake of a Plunging Airfoil," *AIAA Journal*, Vol. 42, No. 10, 2004, pp. 2042–2052. https://doi.org/10.2514/1.5070.